

# Photocurrent in graphene harnessed by tunable intrinsic plasmons

Marcus Freitag<sup>#\*</sup>, Tony Low<sup>#</sup>, Wenjuan Zhu<sup>#</sup>, Huguen Yan, Fengnian Xia, and Phaedon  
Avouris

IBM T.J. Watson Research Center, Yorktown Heights, NY 10598

## Abstract

Graphene's optical properties in the infrared and terahertz can be tailored and enhanced by patterning graphene into periodic metamaterials with sub-wavelength feature sizes. Here we demonstrate polarization sensitive and gate tunable photodetection in graphene nanoribbon arrays. The long-lived hybrid plasmon-phonon modes utilized are coupled excitations of electron density oscillations and substrate ( $\text{SiO}_2$ ) surface polar phonons. Their excitation by s-polarization leads to an in-resonance photocurrent an order of magnitude larger than the photocurrent observed for p-polarization, which excites electron-hole pairs. The plasmonic detectors exhibit photoinduced temperature increases up to four times as large as comparable 2D graphene detectors. Moreover, the photocurrent sign becomes polarization sensitive in the narrowest nanoribbon arrays due to differences in decay channels for photoexcited hybrid plasmon-phonons and electrons. Our work provides a path to light sensitive and frequency selective photodetectors based on graphene's plasmonic excitations.

<sup>#</sup> These authors contributed equally.

<sup>\*</sup> Email: mfreitag@us.ibm.com

Graphene photodetectors rely on graphene for the absorption of light as well as the generation of an electrical signal through photovoltaic,<sup>1-5</sup> thermoelectric,<sup>6-9</sup> or bolometric<sup>10-12</sup> mechanisms. However, the limited absorption in a single layer of graphene through inter-band transitions presents a key challenge.<sup>13</sup> Efforts to increase absorption include building microcavities around graphene<sup>14,15</sup> or enhancing the interaction with light through fabrication of quantum dots,<sup>16</sup> bowtie antennas,<sup>17</sup> and other plasmonic nanostructures on top of the graphene.<sup>18-20</sup> Utilizing the Drude response of free electrons in combination with heavy chemical doping, an increased absorption reaching 40% in a single graphene layer has been achieved in the far-infrared.<sup>21</sup> Graphene with a moderate doping is usually very transparent in the mid-infrared wavelength range. However, the excitation of intrinsic graphene plasmons allows the tuning of strong absorption into the mid-infrared.<sup>22-24</sup> Intrinsic graphene plasmons also produce high confinement of electromagnetic energy in sub-wavelength dimensions in combination with a longer lifetime of the excitation as compared to plasmons in metals.<sup>25</sup> Moreover, unlike surface plasmons in metals,<sup>18-20,26</sup> plasmons in graphene can be effectively tuned with a backgate voltage, potentially enabling optoelectronic switching devices.

In order to excite graphene plasmons with electromagnetic radiation, the wave-vector and energy of plasmon and optical fields have to be matched, which can be done by light scattering from nearby nanostructures,<sup>27</sup> coupling by a grating fabricated on top or below the graphene,<sup>28</sup> or by patterning the graphene into periodic plasmonic meta-materials.<sup>29-31</sup> The latter approach is both simple and flexible in light of modern micro- and nano-fabrication techniques that allow sculpting graphene into a multitude of graphene superstructures. Arrays of graphene nanoribbons (GNR), nanodiscs, or nanorings can all support standing plasmons and can act as sharp notch filters in the mid-infrared, while staying more than 97% transparent elsewhere.<sup>29-31</sup> The dimensions, doping, and to a lesser degree spacing between graphene nanostructures, determine the position of the plasmon resonance and thus the absorption peak.

Here, we incorporate arrays of graphene nanoribbons, supporting standing plasmon excitations, as the active elements in graphene photodetectors. The graphene

plasmons interact with surface polar phonons of the  $\text{SiO}_2$  substrate forming long-lived hybrid plasmon-phonon modes with narrow spectral widths that allow efficient tuning of the mode by simple application of a gate voltage. The plasmon-phonon mode is excited in the mid-infrared exclusively under s-polarization and upon its decay, electron and phonon temperatures in graphene are raised. The elevated temperatures can then result in changes in the electrical conductivity and thus a photocurrent. We distinguish between the effects of the phonon temperature ( $T_{\text{ph}}$ ) on the one hand and the electron temperature ( $T_e$ ) on the other: an increase in  $T_{\text{ph}}$  leads to increased carrier-phonon scattering and a reduction in transport current (reduction mode), while an increase in  $T_e$  is equivalent to an increased carrier density and leads to an increase in transport current (enhancement mode). Despite being a first demonstration of the intrinsic plasmonic-optoelectronic response in graphene meta-materials, our plasmon-enhancement of the photoresponse reaches an order of magnitude under ambient conditions. We emphasize that the physical mechanism of enhancement reported here is fundamentally different from those in previously demonstrated integrated graphene photodetectors with metallic plasmonic structures.<sup>16,18-20</sup> Here, intrinsic graphene plasmonic properties are utilized, allowing for widely tunable plasmon resonance and light detection in the mid-infrared, an important wavelength range for a variety of crucial security, imaging, and sensing applications.

## Results

**Standing plasmons in graphene superstructures.** Our photodetectors consist of GNR arrays with GNR widths between 80nm and 200nm, allowing us to match the standing plasmon resonance of the GNR array to the mid-IR wavelength provided by a  $\text{CO}_2$  laser (10.6 $\mu\text{m}$  wavelength or a frequency of 943 $\text{cm}^{-1}$ ). GNR arrays also impart on the device strong polarization anisotropy, where light polarized perpendicular to the GNR axis (s-pol.) can excite the plasmon, whereas light polarized parallel to the GNR (p-pol.) cannot. This can be used to differentiate between the effects of plasmonic excitations (collective electron density oscillations) and electron-hole pairs (single-particle excitations). An SEM image, a schematic of the experimental setup, and a schematic of the excitation and

decay channels are displayed in Figure 1. Please see the Methods section for the experimental details.

Plasmons are excited when the standing plasmon resonance of the graphene array, tuned by gate modulation of the chemical potential, coincides with a selected incident light frequency. These plasmons decay into hot electron-hole pairs via scattering from the edges of the nanostructures or via inelastic scattering with optical phonons.<sup>25,31</sup> Longer-lived hybrid plasmon-phonon modes that also have narrower spectral widths due to the uncertainty principle, can be induced through coupling with the underlying SiO<sub>2</sub> substrate.<sup>31,32</sup> SiO<sub>2</sub> supports surface polar phonons (SP) that are associated with a temporally changing electric field due to the vibrating positively and negatively charged atoms. On the surface of SiO<sub>2</sub>, this field penetrates outside and thus the SPs can couple to electronic excitations in neighboring materials.<sup>32-34</sup> Graphene is the ultimately thin material and the SP coupling is particularly strong. Decay of hybrid plasmon-phonon modes leads to dissociation into hot electron-hole pairs and substrate SP phonons, which ultimately produce elevated electron and phonon temperatures (see Fig. 1c). Direct decay into graphene optical phonons is precluded under our conditions, since the plasmon-phonon mode that we employ is situated below the optical phonon energy of graphene. Note that the decay channels of hybrid plasmon-phonon quasiparticles and electron-hole pairs are different, which together with the bottleneck for equilibration of electron and phonon temperatures opens up an avenue to control the temperatures of electrons and phonons by polarization.

**Dispersion and doping dependence of hybrid plasmon-phonons.** In freestanding graphene or graphene supported by non-polar surfaces such as diamond-like carbon, the plasmon resonance frequency follows a simple  $\omega \propto \sqrt{q}$  dispersion in the long wavelength limit, with  $q$  being the plasmon wave-vector.<sup>22,35,36</sup> On the other hand, when graphene is placed on a polar substrate such as SiO<sub>2</sub> or hexagonal boron nitride, the surface optical phonons can interact with the electronic degrees of freedom in graphene as described above, leading to coupled plasmon-phonon modes. Hybridization of plasmon and phonon modes alters their character, dispersion, and lifetime.<sup>37-41</sup> Figure 2a

shows an extinction spectrum measured on a GNR superlattice with 160nm wide GNRs. The extinction is defined in terms of the transmission through the array, measured with respect to similar wafers without graphene. Indeed, the extinction spectrum reveals resonances corresponding to the enhanced light absorption due to the excitation of hybrid plasmon-phonon modes that are only observed for polarization perpendicular to the GNRs (s-polarization). Three distinct resonances are observed due to coupling of the graphene plasmon with two prominent surface polar phonons of SiO<sub>2</sub> over the frequency range of interest.

In previous work,<sup>31</sup> we have studied extensively the dispersion of these hybrid plasmon-phonon modes and their associated damping processes in comparison with standard theory based on the Random Phase Approximation (RPA). Figure 3 plots the calculated RPA plasmon loss function  $L(q, \omega)$  in 2D graphene, with details of the models and calculations documented in Supplementary Note 1. Resonance positions of the coupled plasmon-phonon modes are extracted from the measured extinction spectra (symbols). The loss function describes both the plasmon-phonon mode dispersion and their resonance linewidth very well as detailed in Ref.<sup>31</sup>. By slicing the graphene into a superlattice of GNRs each with a physical width of  $w$ , standing plasmons with momentum  $q = \pi/(w - w_0)$  are selected for. The denominator  $w - w_0$  can be interpreted as the electronic width of the GNR, where  $w_0$  is an experimentally determined fitting parameter.<sup>31</sup>

Plasmon-phonon modes are surface electromagnetic waves due to coupled excitations involving both collective electronic (plasmon) and ionic lattice oscillations (phonon). Analogous to a classical coupled harmonic oscillator problem, the nature and quality of the coupled mode (i.e. phonon- or plasmon-like) depends on its resonant frequency. For example, a coupled mode resonating at frequency close to that of the SiO<sub>2</sub> surface polar phonon would exhibit narrow spectral width, inherited from the relatively long sub-picoseconds phonon lifetime.<sup>30</sup> Under certain physical situations, it is necessary to estimate the relative electromagnetic energy content distributed between the plasmon and phonon “oscillators”. For example, electron scattering with coupled plasmon-phonon

mode<sup>32</sup> requires the knowledge of plasmon and phonon content as only the latter amounts to electron's momentum relaxation. Here, we are interested in the plasmonic energy flow into the electronic and phononic baths, which drives the optoelectronic response in graphene. Over the range of energies  $E$  sampled in our experiments, we estimated the constituent electromagnetic energy content to be  $\sim 30\text{-}40\%$  plasmon and  $\sim 60\text{-}70\%$  phonon contents (see Supplementary Figure S1).

The plasmon-phonon mode whose frequency resides within the frequencies of the two  $\text{SiO}_2$  surface polar phonons is shifted by chemical doping within the interval given by the two surface polar phonons  $\omega_{\text{sp1}}$  and  $\omega_{\text{sp2}}$  ( $\sim 800\text{cm}^{-1}$  to  $1100\text{cm}^{-1}$ ) (Figs. 2b,c). We plot the resonance frequency position of this mode as a function of gate voltage tuning for devices with different ribbon width in Fig. 2e. Our gate coupling allows for modulation of the Fermi energy within a  $300\text{meV}$  window. In conjunction with the sub-picoseconds lifetime of this hybrid plasmon-phonon mode, which translates to a broadening of  $\sim 100\text{meV}$ , this should allow for gate-controlled switching of the plasmonic effect. At a photo-excitation frequency of  $\sim 943\text{cm}^{-1}$  as indicated, our extinction measurements (Fig. 2d) and calculation (Fig. 2f) indeed suggest sufficient modulation of the plasmon loss function via gate voltage tuning for GNR superlattices with GNR width of  $140\text{nm}$  and below.

**Plasmon-enhanced photoresponse.** Let us now first inspect the photoresponse of GNR superlattices with a fixed nanoribbon width of  $140\text{nm}$ . These superlattices display a large plasmonic photocurrent at a gate voltage near  $V_G = -35\text{V}$  as can be seen in Fig. 4a. Coupling of photons to the hybrid plasmon-phonon quasi particle is revealed by the order of magnitude increase in photocurrent for s-polarization (polarization perpendicular to the GNRs axis), and the strongly peaked gate-voltage characteristic of the photocurrent, in good agreement with the loss function for  $140\text{nm}$  GNR superlattices calculated in Fig. 2f. The plasmonic photocurrent has a full-width at half maximum of  $\sim 40\text{V}$  in gate voltage, which translate to  $\sim 100\text{meV}$  in energy. This energy window can be made even smaller through improvements in electron mobility. Infrared light with p-polarization does not excite the standing plasmon, and the resulting weak photocurrent is due to the excitation

and subsequent decay of electron-hole pairs. Note that the photocurrent has negative sign throughout the gate voltage range. This reduction mode photoconductivity is dominated by increased carrier scattering with photo-induced phonon temperature.<sup>12</sup> A spatial map of the plasmon-enhanced photoresponse is shown in the inset. The 30 $\mu\text{m}$  x 10 $\mu\text{m}$  GNR superlattice cannot be spatially resolved, because of the long wavelength of the CO<sub>2</sub>-laser photons, limiting our resolution to about 20 $\mu\text{m}$ . Figure 4c plots the polarization angle-dependence of the photocurrent, which follows a standard sine-square behavior:

$$I_{\text{PC}} = I_{\text{Plasmon}} \sin^2(\varphi \cdot \pi/180) + I_{\text{e-h}} \quad (1)$$

Here  $I_{\text{Plasmon}}$  and  $I_{\text{e-h}}$  are the photocurrents due to the plasmon-phonon mode and electron-hole pairs respectively, and  $\varphi$  is the polarization angle, defined as  $\varphi = 0^\circ$  for p-polarization. Enhanced light absorption due to localized plasmons and their subsequent decay primarily into phonons is responsible for the observed enhancement factor  $\beta = |I_{90^\circ}/I_{0^\circ}|$  on the order of  $\sim 15$ , to be discussed.

A comparison between the photoresponse of a GNR superlattice and 2D graphene of the same overall dimension (30 $\mu\text{m}$  x 10 $\mu\text{m}$ ) is shown in Figs. 4d,e. The peak responsivity of the 140nm GNR superlattice is slightly larger than that of 2D graphene. Note that this quantity can easily be increased in both cases by increasing the drain voltage, making the device shorter, or increasing the thermal resistance of the gate stack. By calibrating with the very different transport currents and plotting  $\Delta G/G$  instead (Supplementary Figure S2), a 6 times larger response for the GNR superlattice is obtained. ( $G$  is the conductance and  $\Delta G = I_{\text{ph}}/V_{\text{D}}$  is the photoconductance). We can go a step further and extract the lattice temperature increase upon photoexcitation by measuring the temperature dependence of the transport current in a cryostat around room temperature:  $\Delta G/(G \cdot \Delta T_{\text{ph}}) = -3.1 \cdot 10^{-4} \text{ K}^{-1}$  and  $\Delta G/(G \cdot \Delta T_{\text{ph}}) = -2.5 \cdot 10^{-4} \text{ K}^{-1}$  for 140nm GNRs and 2D graphene respectively. Here  $\Delta T_{\text{ph}}$  is the lattice temperature increase. The resulting curves are plotted in Fig. 4e. Within the plasmon-phonon resonance, the superlattice shows a lattice temperature increase of 3.1K above room temperature, while the 2D graphene lattice temperature increase is flat at 0.7K. Typical absorption for

graphene superlattices on the order of 5% (Fig. 2d) and for 2D graphene in the Pauli blocking regime around 1% are consistent with these temperature increases inferred from the photocurrents.

The drain-voltage dependence of the plasmon-enhanced photocurrent (Fig. 4f) shows saturation starting at 8V of source-drain bias corresponding to 0.26 V/ $\mu\text{m}$  on average. The associated decrease in photoconductance  $\Delta G$  (Supplementary Figure S3) is partly due to the increased temperature stemming from Joule heating and partly due to inhomogeneous broadening of the plasmon resonance due to the potential gradient along the graphene at higher drain voltages. To first order, the deposited electrical power  $P_{\text{el}} = |V_{\text{D}} \cdot I|$  is proportional to the increased device temperature relative to its ambient, denoted as  $\Delta T_{\text{Joule}}$ . A simple estimate based on our previous work suggests  $\Delta T_{\text{Joule}}/P_{\text{el}} \sim 10^3 \text{ KW}^{-1}$  for  $30\mu\text{m} \times 10\mu\text{m}$  large devices.<sup>42</sup> Source-drain voltages between 2 and 20V correspond to deposited electrical powers between 1 and 60mW, and temperature increases between 1 and 60K. We can identify two contributions to the decrease in photoconductance with Joule heating, both discussed in more detail in the Supplementary Figure S3. First, Joule heating leads to an increase in the out-of-plane thermal conductance of graphene due to the  $\text{SiO}_2/\text{Si}$  gate stack  $\kappa_0$ , which reduces the photo-induced lattice temperature increase  $\Delta T_{\text{ph}}$  through  $\Delta T_{\text{ph}} = P_{\text{ph}}/\kappa_0$ , where  $P_{\text{ph}}$  is the absorbed power by the phonon bath. Second, Joule heating also leads to a broadening of the gate voltage tuned plasmonic photocurrent peak due to a reduction in plasmon lifetime. This effect is small however, less than 10% for 10V source-drain bias.

**Dual tunability of plasmonic graphene photodetectors.** We now turn to the GNR width dependence of the plasmon-enhanced photocurrent, which lets us tune the peak photoresponse in addition to gate-voltage tuning. Figure 5 plots the experimental photocurrent under polarization normal to the GNR axis, as well as the photocurrent enhancement factor  $\beta = |I_{90^\circ}/I_{0^\circ}|$  for GNR superlattices of different widths. The photocurrent enhancement factors can be compared to the modeled absorption peaks in



Fig. 2f. Both the 140nm and 120nm photocurrent peaks match very well with the corresponding maxima in the loss function. In 200nm and 160nm GNRs the photocurrent peak resides outside our experimental range of  $V_G = -40\text{V}$  to  $40\text{V}$  in both theory and experiment. For the smallest GNRs with width of 100nm and below however, the photocurrent peak is weaker and shifted as compared to the modeled absorption peak. Interestingly, we also observe inversion of the photocurrent direction in 100nm and 80nm GNR arrays at positive gate voltages, and a distinct photocurrent polarity dependence on the polarization of the incident light at certain gate voltages as indicated by the brown shaded regions in Fig. 6. We proceed to discuss the photocurrent generation mechanisms in order to explain these observations.

## Discussion

Biased photodetectors either work in a mode where the transport current is enhanced or reduced due to the absorbed energy. Enhancement, prominent in semiconductor bolometers including gapped bilayer graphene,<sup>11</sup> is promoted by the conduction of the photo-generated carriers and can be described in graphene by a hot electron temperature  $T_e$  (refs <sup>8,9</sup>), while reduction is mediated through the phonon-limited mobility, and thus can be described by the raised lattice temperature  $T_{ph}$ . Enhancement dominates in graphene at low doping close to the Dirac point, while reduction dominates at high doping.<sup>12</sup> Since our GNR superlattices are strongly p-doped, with an estimated Dirac point at  $V_G=52\text{V}$ , reduction due to increased phonon scattering usually dominates. Indeed, 120nm, 140nm, 160nm, and 200nm wide GNR superlattices show the reduction mode throughout the gate voltage range from  $-40\text{V}$  to  $40\text{V}$ , and Fig. 4c plots the corresponding lattice temperature increase  $\Delta T_{ph}$  in the case of the 140nm GNR superlattice.

In narrower GNRs with widths around 100nm and below however, the situation is different. Here disordered edges lead to a thermally-activated hopping transport along localized states with size close to the GNR width.<sup>43</sup> The resulting transport gap (or mobility gap) on the order of 100meV is not to be confused with a real bandgap, which

becomes important only for much narrower GNRs below 10nm (ref. <sup>44</sup>), or in bilayer graphene,<sup>11</sup> where the bandgap is even tunable by a perpendicular electric field. In GNRs, the energy scale of the transport gap derives from both localization and charging, and translates into a gate voltage window of a few volts around the Dirac point. The activation energy for hopping transport within the transport gap is on the order of 10meV (ref. <sup>43</sup>), suggesting that an increase in electron temperature upon photoexcitation should lead to a positive photocurrent when biased in the vicinity of the mobility gap gate-voltage region. Thus we would expect that we see a transition from reduction mode to enhancement mode in small-width GNRs, and that this transition moves to more negative gate voltages for narrower GNRs. In our experiments we indeed observe a positive photocurrent in 100nm wide GNR arrays above  $V_G=10V$ , and in 80nm wide GNR arrays above  $V_G=-20V$  (see Figs. 5 and 6).

An interesting situation occurs when the position of the plasmonic absorption peak, which moves to more positive gate voltages as the nanoribbon width is reduced, crosses over from reduction mode to enhancement mode. In 100nm wide GNR arrays, the plasmonic absorption peak (Fig. 2f) lies in a region of reduced photosensitivity due to the competition between reduction mode and enhancement mode photoconductivity. This certainly contributes to the comparatively small enhancement factor  $\beta \sim 5$  in 100nm GNRs, in combination with a broadening of the plasmon peak due to edge scattering.<sup>31</sup>

In 80nm wide GNR arrays (Fig. 6f) the plasmon peak has become very broad due to edge scattering, so that plasmon enhancement extends over a wide gate-voltage range in both reduction mode and enhancement mode regions. It is in these narrowest of our GNRs where we observe a switch in photocurrent sign as a function of incident light polarization in addition to gate voltage. P-polarized light excites electron-hole pairs, which decay through electron-electron scattering, effectively multiplying the primary photocarriers, and leading to an enhancement-mode photocurrent due to the increased electron temperature (see also the schematic in Fig. 1c). Thermalization with phonons is hindered through an electron-phonon scattering bottleneck.<sup>8,9</sup> S-polarized light on the other hand, excites the hybrid plasmon-phonon mode, which decays mainly into phonons

due to the 65% phonon character of this mode. This increases electron-phonon scattering (reduction mode) and leads to a photocurrent in the opposite direction. The photocurrent sign, not only the magnitude therefore depends on the polarization of the incident light within a gate-voltage range where enhancement and reduction mode photoconductivity are of the same order. As far as we know, the photocurrent polarity change with polarization has not been reported in any other material system before. It is a consequence of the competition between enhancement mode, which is favored by the decay of electron-hole pairs, and reduction mode, which is favored by the decay of the hybrid plasmon-phonon quasiparticles.

In conclusion, we present a novel room-temperature mid-infrared detector based on the intrinsic graphene plasmon excitations. Graphene plasmons are longer lived than their counterparts in metals because of the superior mobility in graphene. We further alter the graphene plasmons by remote plasmon-phonon coupling with the surface phonons of the polar substrate. The hybrid plasmon-phonon modes are even longer lived and highly gate tunable. We obtain very promising plasmonic enhancement factors with GNR superlattice photodetectors, exceeding an order of magnitude as compared to excitation of electron-hole pairs alone. The general principle can be applied to engineering graphene photodetectors for applications over very wide spectra from terahertz to infrared frequencies. Future improvements include low temperature operation, device geometry optimizations, interdigitated finger electrodes, access to the higher energy plasmon-phonon mode whose wavefunction has higher plasmon character, and more effective grating structures instead of nanoribbons that preserve graphene's intrinsic high mobility.

## Methods

**Sample preparation.** Single-layer graphene (see Supplementary Figure S4) is grown by CVD on copper foil.<sup>45</sup> The copper is dissolved in etchant CE200 and the free-floating graphene is transferred to a silicon chip with 90nm SiO<sub>2</sub>. Graphene devices 30μm long and 10μm wide, as well as the 1/20/40 nm Ti/Pd/Au contacts are fabricated by e-beam lithography. In a final step, the 2D graphene is etched into GNR superlattices by e-beam lithography with PMMA resist and oxygen plasma. The nanoribbon widths range from 80nm to 200nm. The fill factor (width/period=1/2) is kept constant throughout.

**Experimental details.** GNR superlattice photodetectors are illuminated by a focused and chopped CO<sub>2</sub> laser beam at  $\lambda = 10.6\mu\text{m}$  or  $\omega = 943\text{cm}^{-1}$ . We use a ZnSe objective to focus the laser to a spot 20μm in diameter. The laser power is 66mW, corresponding to a moderate power density on the order of  $2 \cdot 10^4 \text{Wcm}^{-2}$ . In plasmon-enhanced photodetectors, the typical p-n junction geometry would be undesirable, since junctions include doping gradients that lead to shifts in plasmon frequencies, broadening the phonon-plasmon peaks. Therefore, we chose to apply a small drain bias of -2V (corresponding to an average electric field of  $670\text{Vcm}^{-1}$ ) keeping the electrostatic doping almost constant throughout. The source side is connected to a preamplifier and lock-in detector, referenced to the chopping frequency of the mechanical chopper at 1.1KHz (Fig. 1c). The RMS values of the photocurrent amplitude at the lock-in output are translated to peak-to-peak values for the manuscript. Measurements are performed in air and the electrical characteristic of the GNR superlattice photodetectors are p-type (Supplementary Figure S5) with residual doping corresponding to a Fermi Level of  $E_F = 0.33\text{eV}$ . A global Si backgate is used to tune the Fermi level.

## Acknowledgements

The authors thank B. Ek and J. Bucchignano for help with device fabrication.

## References

- 1 Lee, E. J. H., Balasubramanian, K., Weitz, R. T., Burghard, M. & Kern, K. Contact and edge effects in graphene devices. *Nature Nanotech.* **3**, 486-490 (2008).
- 2 Mueller, T., Xia, F., Freitag, M., Tsang, J. & Avouris, P. Role of contacts in graphene transistors: A scanning photocurrent study. *Phys. Rev. B* **79**, 245430 (2009).
- 3 Xia, F. *et al.* Photocurrent Imaging and Efficient Photon Detection in a Graphene Transistor. *Nano Lett.* **9**, 1039-1044 (2009).
- 4 Peters, E. C., Lee, E. J., Burghard, M. & Kern, K. Gate dependent photocurrents at a graphene p-n junction. *Appl. Phys. Lett.* **97**, 193102 (2010).
- 5 Rao, G., Freitag, M., Chiu, H.-Y., Sundaram, R. S. & Avouris, P. Raman and Photocurrent Imaging of Electrical Stress-Induced p-n Junctions in Graphene. *ACS Nano* **5**, 5848-5854 (2011).
- 6 Xu, X., Gabor, N. M., Alden, J. S., van der Zande, A. M. & McEuen, P. L. Photo-Thermoelectric Effect at a Graphene Interface Junction. *Nano Lett.* **10**, 562-566 (2009).
- 7 Lemme, M. C. *et al.* Gate-Activated Photoresponse in a Graphene p-n Junction. *Nano Lett.* **11**, 4134-4137 (2011).
- 8 Song, J. C. W., Rudner, M. S., Marcus, C. M. & Levitov, L. S. Hot Carrier Transport and Photocurrent Response in Graphene. *Nano Lett.* **11**, 4688-4692 (2011).
- 9 Gabor, N. M. *et al.* Hot Carrier-Assisted Intrinsic Photoresponse in Graphene. *Science* **334**, 648-652 (2011).
- 10 Vora, H., Kumaravadivel, P., Nielsen, B. & Du, X. Bolometric response in graphene based superconducting tunnel junctions. *Appl. Phys. Lett.* **100**, 153507 (2012).
- 11 Yan, J. *et al.* Dual-gated bilayer graphene hot-electron bolometer. *Nature Nanotech.* **7**, 472-478 (2012).

- 12 Freitag, M., Low, T., Xia, F. & Avouris, P. Photoconductivity of biased graphene. *Nature Photonics* **7**, 53-59 (2013).
- 13 Nair, R. R. *et al.* Fine Structure Constant Defines Visual Transparency of Graphene. *Science* **320**, 1308 (2008).
- 14 Engel, M. *et al.* Light-matter interaction in a microcavity-controlled graphene transistor. *Nature Commun.* **3**, 906 (2012).
- 15 Furchi, M. *et al.* Microcavity-Integrated Graphene Photodetector. *Nano Lett.* **12**, 2773-2777 (2012).
- 16 Konstantatos, G. *et al.* Hybrid graphene-quantum dot phototransistors with ultrahigh gain. *Nature Nanotech.* **7**, 363-368 (2012).
- 17 Emani, N. K. *et al.* Electrically Tunable Damping of Plasmonic Resonances with Graphene. *Nano Lett.* **12**, 5202-5206 (2012).
- 18 Echtermeyer, T. J. *et al.* Strong plasmonic enhancement of photovoltage in graphene. *Nature Commun.* **2**, 458 (2011).
- 19 Liu, Y. *et al.* Plasmon resonance enhanced multicolour photodetection by graphene. *Nature Commun.* **2**, 579 (2011).
- 20 Shi, S. F., Xu, X., Ralph, D. C. & McEuen, P. L. Plasmon Resonance in Individual Nanogap Electrodes Studied Using Graphene Nanoconstrictions as Photodetectors. *Nano Lett.* **11**, 1814-1818 (2011).
- 21 Yan, H. *et al.* Infrared Spectroscopy of Wafer-Scale Graphene. *ACS Nano* **5**, 9854-9860 (2011).
- 22 Hwang, E. H. & Das Sarma, S. Dielectric function, screening, and plasmons in two-dimensional graphene. *Phys. Rev. B* **75**, 205418 (2007).
- 23 Chen, J. *et al.* Optical nano-imaging of gate-tunable graphene plasmons. *Nature* **487**, 77-81 (2012).
- 24 Grigorenko, A. N., Polini, M. & Novoselov, K. S. Graphene plasmonics. *Nature Photonics* **6**, 749-758 (2012).
- 25 Jablan, M., Soljacic, M. & Buljan, H. Unconventional plasmon-phonon coupling in graphene. *Phys. Rev. B* **83**, 161409 (2011).
- 26 Raether, H. Surface Plasmons. (*ed. Hoehler, G.*) Springer, Berlin (1988).

- 27 Fei, Z. *et al.* Infrared Nanoscopy of Dirac Plasmons at the Graphene-SiO<sub>2</sub> Interface. *Nano Lett.* **11**, 4701-4705 (2011).
- 28 Nader Esfahani, N. *et al.* Plasmon absorption in grating-coupled InP HEMT and graphene sheet for tunable THz Detection. *Proc. SPIE* **8261**, Terahertz Technology and Applications V, 82610E (2012).
- 29 Ju, L. *et al.* Graphene plasmonics for tunable terahertz metamaterials. *Nature Nanotech.* **6**, 630-634 (2011).
- 30 Yan, H. *et al.* Tunable infrared plasmonic devices using graphene/insulator stacks. *Nature Nanotech.* **7**, 330-334 (2012).
- 31 Yan, H. *et al.* Damping pathways of mid-infrared plasmons in graphene nanostructures. *Nature Photonics*, doi: 10.1038/nphoton.2013.1057 (published online 14 April 2013).
- 32 Fischetti, M. V., Neumayer, D. A. & Cartier, E. A. Effective electron mobility in Si inversion layers in metal-oxide-semiconductor systems with a high-kappa insulator: The role of remote phonon scattering. *Journal of Applied Physics* **90**, 4587-4608 (2001).
- 33 Chen, J.-H., Jang, C., Xiao, S., Ishigami, M. & Fuhrer, M. S. Intrinsic and extrinsic performance limits of graphene devices on SiO<sub>2</sub>. *Nature Nanotech.* **3**, 206-209 (2008).
- 34 Zhu, W., Perebeinos, V., Freitag, M. & Avouris, P. Carrier scattering, mobilities, and electrostatic potential in monolayer, bilayer, and trilayer graphene. *Phys. Rev. B* **80**, 235402 (2009).
- 35 Stern, F. Polarizability of a Two-Dimensional Electron Gas. *Phys. Rev. Lett.* **18**, 546-548 (1967).
- 36 Wunsch, B., Stauber, T., Sols, F. & Guinea, F. Dynamical polarization of graphene at finite doping. *New Journal of Physics* **8**, 318 (2006).
- 37 Dubois, L. H. & Schwartz, G. P. Surface optical phonons and hydrogen chemisorption on polar and nonpolar faces of GaAs, InP, and GaP. *Phys. Rev. B* **26**, 794-802 (1982).
- 38 Matz, R. & Lueth, H. Conduction-Band Surface Plasmons in the Electron-Energy-Loss Spectrum of GaAs(110). *Phys. Rev. Lett.* **46**, 500-503 (1981).

- 39 Wang, S. Q. & Mahan, G. D. Electron Scattering from Surface Excitations. *Phys. Rev. B* **6**, 4517-4524 (1972).
- 40 Fratini, S. & Guinea, F. Substrate-limited electron dynamics in graphene. *Phys. Rev. B* **77**, 195415 (2008).
- 41 Hwang, E. H., Sensarma, R. & Das Sarma, S. Plasmon-phonon coupling in graphene. *Phys. Rev. B* **82**, 195406 (2010).
- 42 Freitag, M. *et al.* Energy Dissipation in Graphene Field-Effect Transistors. *Nano Lett.* **9**, 1883-1888 (2009).
- 43 Han, M. Y., Brant, J. C. & Kim, P. Electron Transport in Disordered Graphene Nanoribbons. *Phys. Rev. Lett.* **104**, 056801 (2010).
- 44 Li, X., Wang, X., Zhang, L., Lee, S. & Dai, H. Chemically Derived, Ultrasoft Graphene Nanoribbon Semiconductors. *Science* **319**, 1229-1232 (2008).
- 45 Li, X. *et al.* Large-Area Synthesis of High-Quality and Uniform Graphene Films on Copper Foils. *Science* **324**, 1312-1314 (2009).



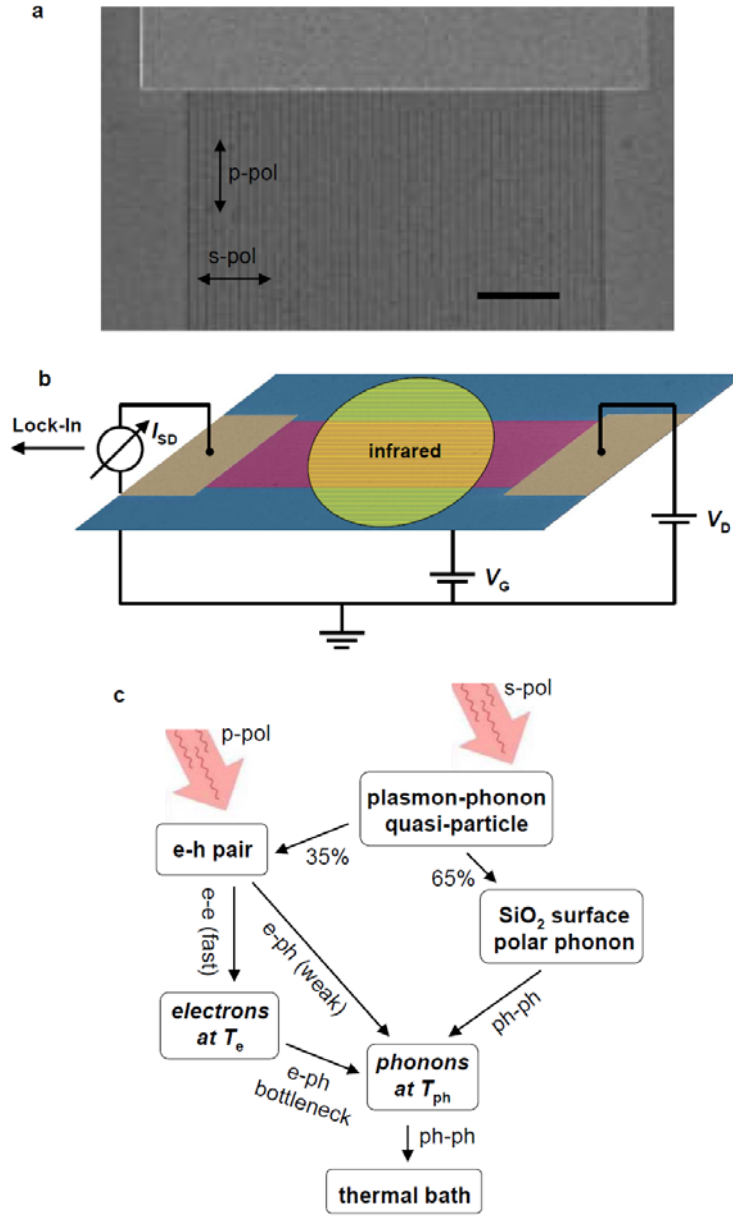


**Figure 1: Graphene nanoribbon superlattice photodetector.** (a) SEM close-up of the contact area of a graphene nanoribbon array photodetector with 100 nm GNR width and 100 nm GNR spacing. (Scale bar is 2 $\mu\text{m}$ ). The length and width of the entire array are 30 $\mu\text{m}$  and 10 $\mu\text{m}$  respectively. (b) Schematic of the photoconductivity setup. Infrared laser light at 10.6 $\mu\text{m}$  is chopped at 1.1KHz and the photocurrent is analyzed by a lock-in amplifier referenced to the chopping frequency. (c) Illustration of the mechanism of phonon and hot electron generation through decay of the hybrid plasmon-phonon quasi-

particles. S-polarized infrared light excites primarily the plasmon-phonon mode, while p-polarized light excites individual electron-hole pairs. The plasmon-phonon quasi-particle decays mainly through surface polar phonons into other phonons, while electron-hole pairs decay primarily into hot electrons. Electrons thermalize among themselves at a temperature  $T_e$ , and phonons among themselves at a temperature  $T_{ph}$ . A bottleneck exists between electron and phonon baths, preventing full thermalization of electrons and phonons in graphene. This is especially important for the decay of electron-hole pairs excited with p-polarization. The type of scattering (electron-electron, electron-phonon, or phonon-phonon) is indicated.

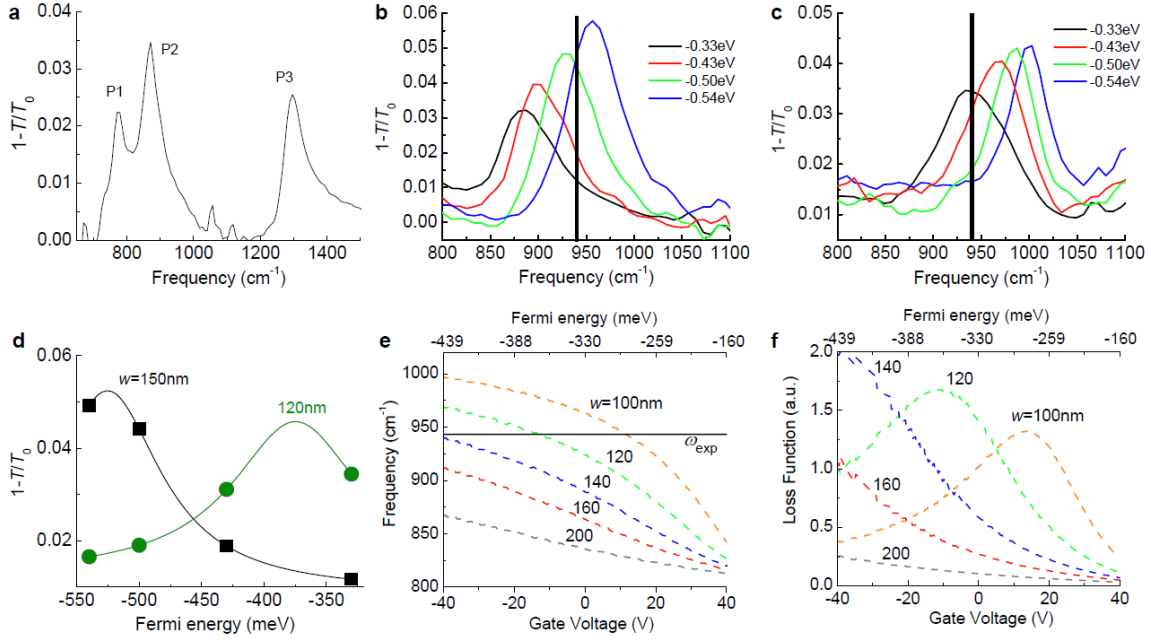


**Figure 2: Hybrid plasmon-phonon modes generated through coupling of graphene plasmons and SiO<sub>2</sub> surface polar phonons.** (a) Extinction spectrum of a 160nm GNR array on SiO<sub>2</sub> in the mid-infrared, measured with an FTIR spectrometer under s-polarization (polarization perpendicular to the GNRs). Three hybrid plasmon-phonon modes can be identified. Their energies are determined by the interaction of the graphene plasmon mode with two surface polar phonons of the SiO<sub>2</sub> underlayer. (b-c) Extinction spectra in the region of the second peak (P2) for GNR arrays with GNR widths of (b) 150nm and (c) 120nm and varying chemical doping (Fermi) levels as indicated. The solid vertical line indicates the energy of the CO<sub>2</sub> laser used in subsequent photocurrent experiments. (d) Extinction as a function of doping, extracted from the two previous plots at the energy of the CO<sub>2</sub> laser, 943cm<sup>-1</sup>. Black squares: 150nm GNRs; Green circles: 120nm GNRs. The solid lines are Lorentzian fits. (e) Calculated plasmon resonance frequency as a function of Fermi energy and gate voltage tuning for GNR arrays of different widths. (f) Calculated plasmon loss function as a function of Fermi energy and gate voltage tuning for GNR arrays of different widths at the experimental frequency of 943cm<sup>-1</sup>.

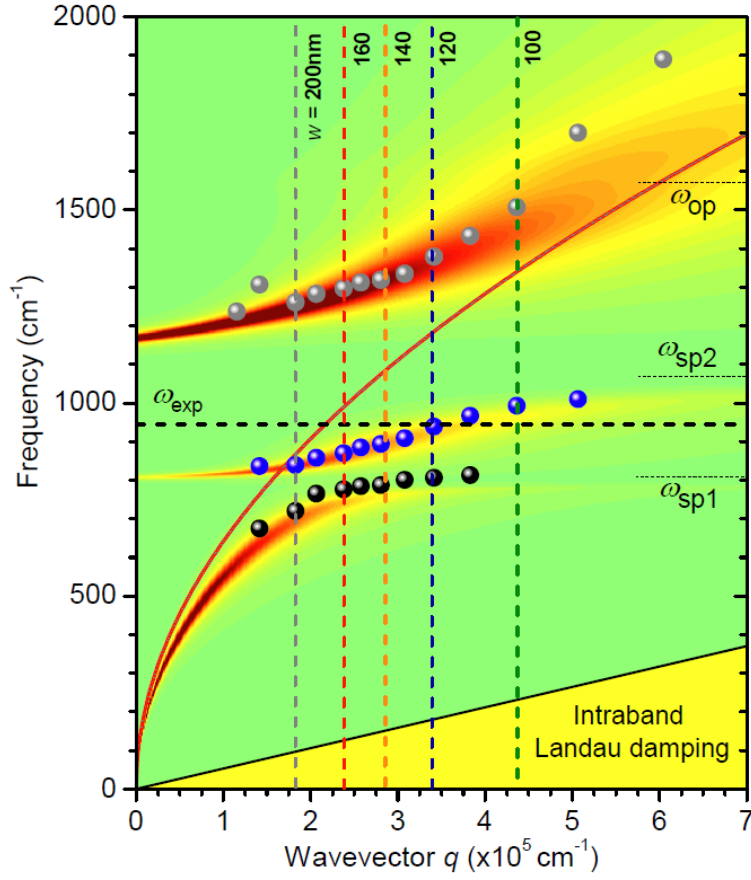


**Figure 3: Graphene's loss function and plasmons.** Color intensity plot of graphene loss function  $L(q, \omega)$  assuming a doping of 0.33 eV. The calculation includes coupling with the intrinsic optical phonon and the two substrate polar phonons of SiO<sub>2</sub> as indicated in the figure. Prominent plasmon damping processes are included in the calculation with models taken from Ref. <sup>30</sup>. See Supplementary Note 1 for details of calculations. Data points are from absorption experiments such as in Fig. 2a.

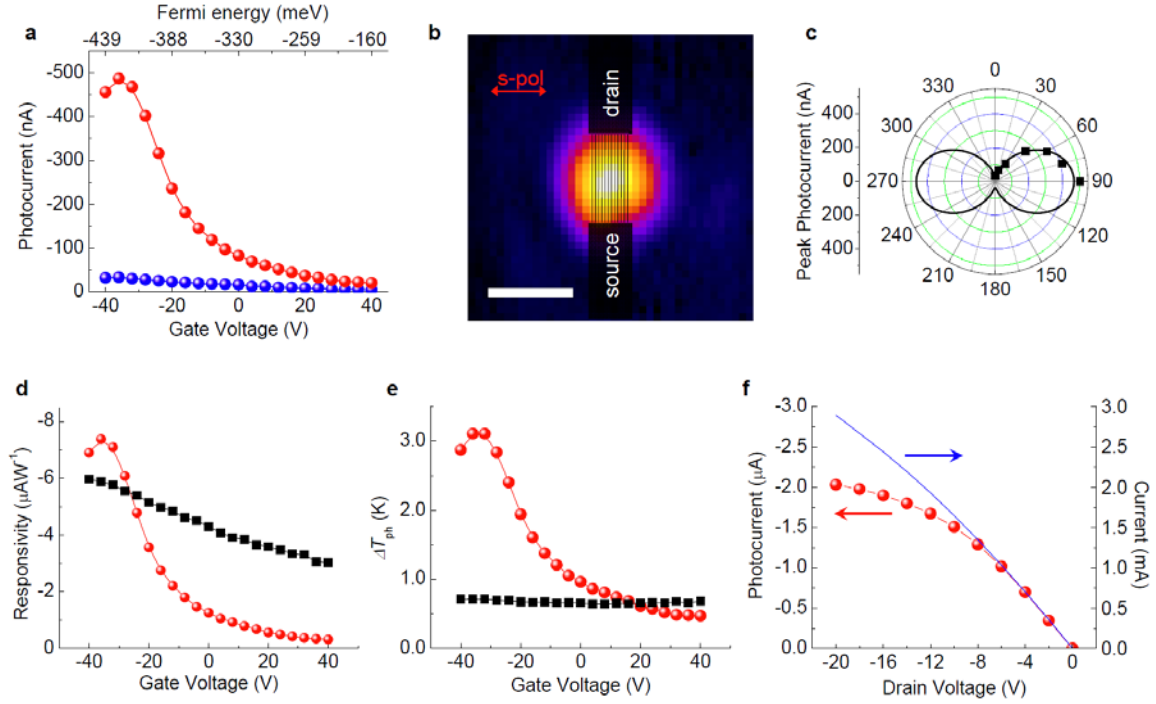


**Figure 4: Plasmon-enhanced graphene superlattice photodetector.** (a) Gate-voltage dependent photocurrent of a superlattice of 140nm GNRs with incident IR light under s-polarization (red spheres) and p-polarization (blue spheres). The corresponding Fermi energies are indicated on top. (Laser power  $P=66\text{mW}$ ; drain voltage  $V_D=-2\text{V}$ ) (b) Scanning photocurrent image of the GNR superlattice photodetector. Scale bar is  $30\mu\text{m}$ . (c) Polarization dependence of the peak photocurrent under the same conditions. (d) Responsivity of 140nm GNR superlattice (red spheres) and 2D graphene (black squares) upon photoexcitation with the same laser power  $P=66\text{mW}$  and drain voltage  $V_D=-2\text{V}$ . (e) Comparison of the lattice temperature increase of 140nm GNR arrays (red spheres) and 2D graphene (black squares) under these conditions. (f) Bias dependence of the photocurrent and transport current in a 140nm GNR superlattice at  $V_G=-40\text{V}$ . Photocurrent saturation sets in above  $V_D=-8\text{V}$ .

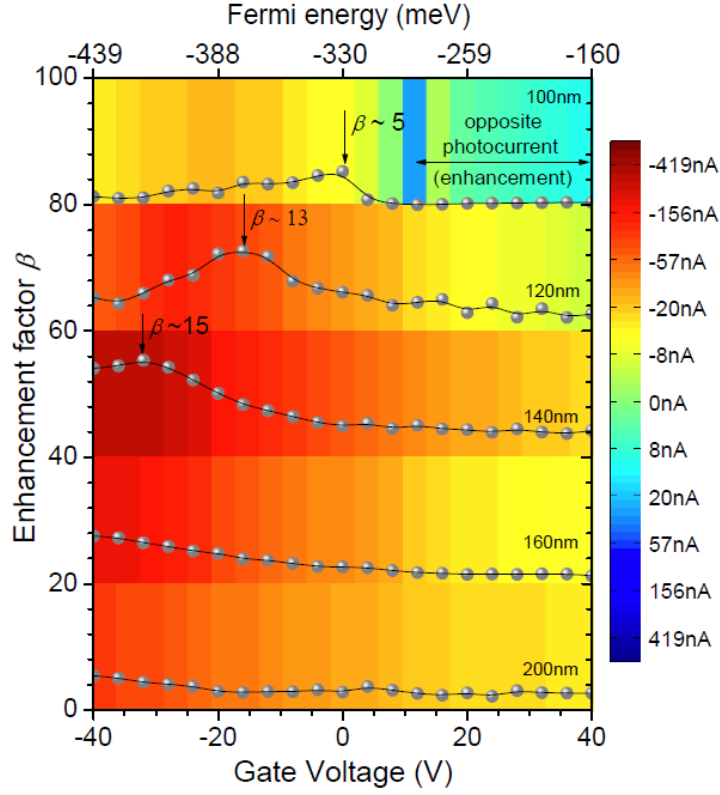


**Figure 5: Photoresponse as a function of gate-voltage tuning and GNR width.** Gate-voltage dependent photocurrent enhancement factor  $\beta = |I_{90^\circ}/I_{0^\circ}|$  for GNR superlattices with different GNR width. Subsequent curves are displaced by 20 units for clarity. Photocurrent enhancement due to the plasmon reaches  $\beta=15$  for 140nm GNR superlattices. **Color coding:** Gate-voltage dependent photocurrent  $I_{ph}$  for these GNR superlattices under s-polarization ( $I_{90^\circ}$ ), plotted on a logarithmic color scale. ( $P=66\text{mW}$ ,  $V_D=-2\text{V}$ ). The entire data set for s- and p-polarization is shown in Fig. 6.

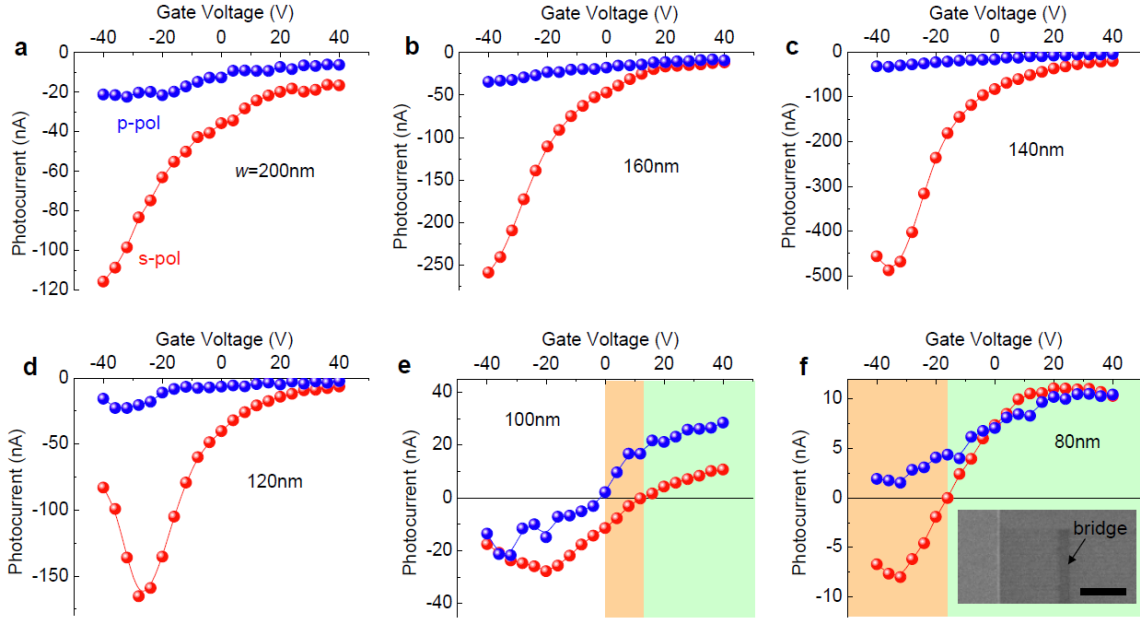


**Figure 6: Photocurrent polarity for varying GNR width.** (a)-(f) Photocurrent under s- and p-polarization as a function of gate voltage tuning for arrays with varying GNR width. ( $P=66\text{mW}$ ,  $V_D=-2\text{V}$ ). For p-polarized light, which does not excite the plasmons, the photocurrent is more negative at negative gate voltages, due to the stronger reduction mode photocurrent at higher electrostatic doping.<sup>12</sup> S-polarized light excites the plasmon-phonon mode and the photocurrents are dominated by the plasmonic response. GNR arrays above 120nm width (a-d) show reduction mode photoconductivity throughout the gate voltage range. The smallest GNRs (100nm and 80nm, (e-f)) exhibit transitions from negative to positive photocurrent with increasing gate voltage due to a switch from reduction mode to enhancement mode photoconductivity. The green shaded gate-voltage regions indicate positive photocurrent. The brown shaded regions highlight the gate voltage ranges where s- and p-polarization yield opposite *sign* of photocurrent. The 80nm GNR array contains 7 graphene bridges perpendicular to the GNRs to guarantee current continuity along the  $30\mu\text{m}$  long GNR array. One of the bridges is shown in the zoomed-in SEM image in the inset in (f). Scale bar is  $2\mu\text{m}$ .

# Supplementary Information: Photocurrent in graphene harnessed by tunable intrinsic plasmons

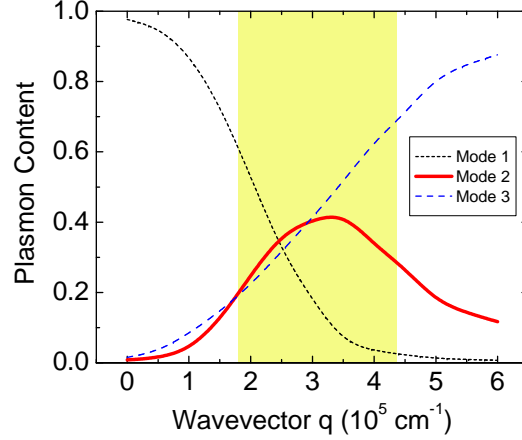
Marcus Freitag<sup>#\*</sup>, Tony Low<sup>#</sup>, Wenjuan Zhu<sup>#</sup>,  
Hugen Yan, Fengnian Xia and Phaedon Avouris  
*IBM T.J. Watson Research Center,  
Yorktown Heights, NY 10598, US*

*(# These authors contributed equally)*

---

\* mfreitag@us.ibm.com





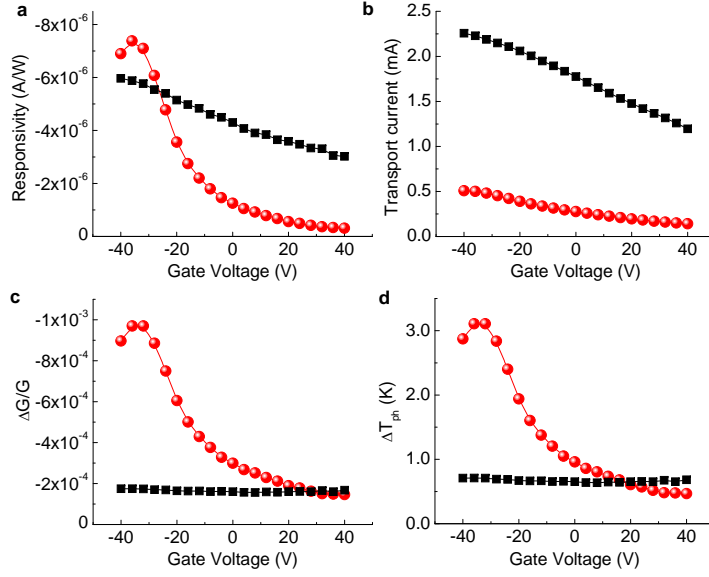
**Supplementary Figure S1: Plasmon content of the three hybrid plasmon-phonon**

**modes.** Estimate based on optically measured resonance frequencies as depicted in Fig. 3 of the main manuscript. Highlighted region indicates the range of  $q$  accessed in our experiments. The plasmon-phonon modes are surface electromagnetic waves due to coupled excitations involving both collective electronic (plasmon) and ionic lattice oscillations (phonon). The resonant frequency of the coupled mode is generally different from its constituent and depends on the coupling strength. Analogous to a classical coupled harmonic oscillator problem, the nature and quality of the coupled mode (i.e. phonon- or plasmon-like) depends on its resonant frequency. For example, a coupled mode resonating at frequency close to that of the SiO<sub>2</sub> surface polar phonon exhibits narrow spectral width, inherited from the relatively long sub-picoseconds phonon lifetime.[31] Under certain physical situations, it is necessary to estimate the relative electromagnetic energy content distributed between the plasmon and phonon “oscillators”. For example, electron scattering with coupled plasmon-phonon mode[32] requires the knowledge of plasmon and phonon content as only the latter amounts to electron’s momentum relaxation. Optoelectronic response in graphene is governed by the various energy dissipation pathways e.g. phonons bath, contacts, substrate.[46,47] Here, we are interested in the plasmonic energy flow into the electronic and phononic baths, which drives the optoelectronic response in graphene. Owing to the hybridization of graphene plasmon with the two surface polar phonon modes, three plasmon-phonon coupled modes can be identified as shown in Fig. 3 in the main text at frequencies  $\omega_1 < \omega_{sp1}$  (“mode 1”),  $\omega_{sp1} < \omega_2 < \omega_{sp2}$  (“mode 2”) and  $\omega_3 > \omega_{sp2}$  (“mode 3”). In this work, we exploit the hybrid plasmon-phonon “mode 2” in our experiments. Subsequent decay of these hybrid modes lead to dissociation into hot electron-hole pairs and substrate

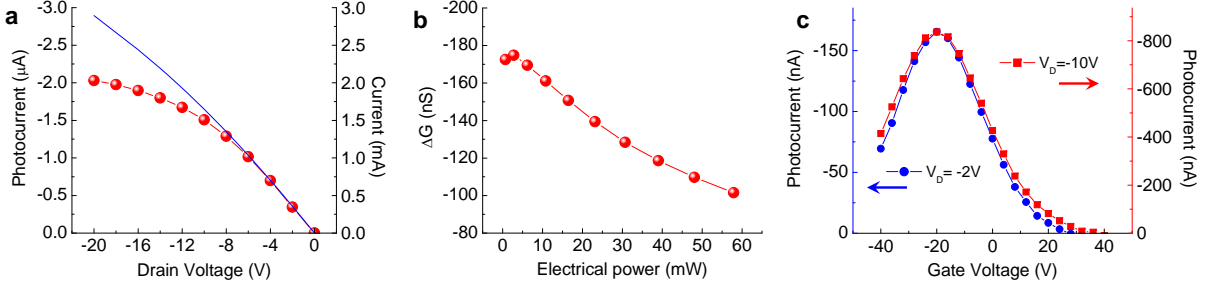
surface phonons, and their relative proportion depends on the plasmon-phonon content of the particular hybrid mode. Following Ref. [32], the plasmon content  $\Phi_j(q)$  for mode  $j$  is estimated using,

$$\Phi_j = \frac{(\omega_j^2 - \omega_{sp1}^2)(\omega_j^2 - \omega_{sp2}^2)}{(\omega_j^2 - \omega_i^2)(\omega_j^2 - \omega_k^2)} \quad (\text{S1})$$

where the indices  $i, j, k$  are cyclical and the sum rule  $\Phi_1 + \Phi_2 + \Phi_3 = 1$  holds. Estimated  $\Phi_j(q)$  for the three hybrid modes are shown above. In particular, we are interested in the plasmon content of “mode 2” over the range of  $q$  accessed in our experiments as indicated by the highlighted region. We see that its plasmon content exceeds 40% for some intermediate  $q$  which corresponds to the 120 and 140 nm ribbons.

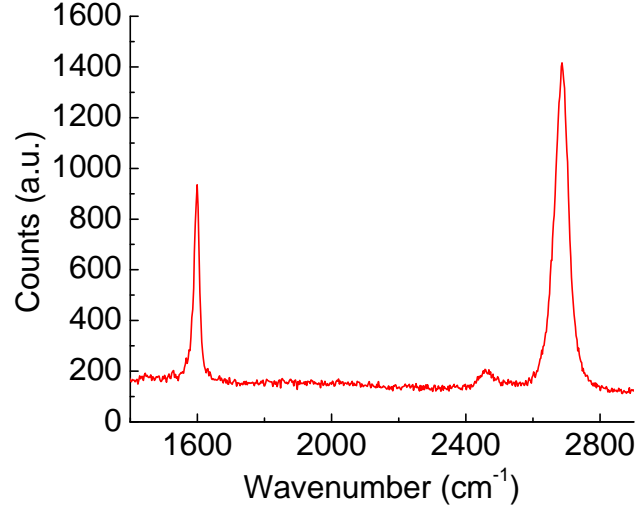


**Supplementary Figure S2: Comparison of GNR superlattice photodetectors with 2D graphene.** The GNR superlattice photodetector (red spheres) and 2D graphene (black squares) have identical dimensions. ( $\lambda = 10.6 \mu\text{m}$ ,  $P = 66 \text{ mW}$ ,  $V_D = -2 \text{ V}$ ). **(a)** The responsivity of 140 nm GNR superlattices is slightly larger than that of 2D graphene, even though it has only 1/2 fill factor. 2D graphene shows a small gradual decrease in photocurrent with gate voltage due to the decrease in transport current, while 140 nm GNR superlattices show a pronounced peak due to the hybrid plasmon-phonon mode. **(b)** 2D graphene has a 5 times larger transport current partly stemming from the reduced graphene coverage in the superlattice, and partly from defects or edge roughness scattering, which makes the area close to the nanoribbon edges less conductive. **(c)** By calibrating with the different transport currents and plotting  $\Delta G/G$  instead, a 6 times larger response for the GNR superlattice is obtained. ( $G$  is the conductance and  $\Delta G = I_{ph}/V_D$  is the photoconductance). **(d)** The quantity  $\Delta G/G$  can be translated into the lattice temperature increase  $\Delta T_{ph}$  by measuring the temperature dependence of the transport current in a cryostat, from which we obtain:  $\frac{\Delta G}{G \cdot \Delta T_{ph}} = -3.1 \cdot 10^{-4} \text{ K}^{-1}$  and  $-2.5 \cdot 10^{-4} \text{ K}^{-1}$  for 140 nm GNRs and 2D graphene respectively. While the gate-voltage dependence of the temperature increase is flat in 2D graphene at 0.7 K, it reaches 3.1 K in 140 nm GNR superlattices in resonance.

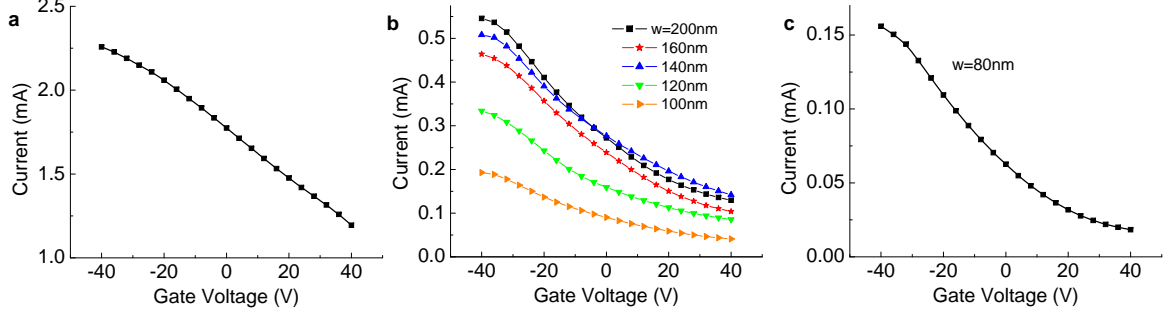


**Supplementary Figure S3: Effects of the drain voltage.** (a) We use a transport current to heat the sample (Joule heating) and measure the AC photocurrent at the same time in a 140nm GNR superlattice at  $V_G = -40$  V near the plasmon-phonon resonance. The temperature increase can be estimated from our previous work on the order of  $\Delta T_{Joule}/P_{el} \approx 1\text{K/mW}$  for  $30\mu\text{m}$  devices.[42] Source-drain voltages between 2 and 20V correspond to deposited electrical powers between 1 and 60mW, and temperature increases between 1 and 60K. Photocurrent saturation sets in above -8V drain voltage, corresponding to a 10K increase in temperature. (b) To analyze this further, we plot the photoconductance  $\Delta G = I_{ph}/V_D$  as a function of deposited electric power  $P_{el}$ . In reduction mode,  $\Delta G$  is proportional to the elevated phonon temperature upon light excitation  $\Delta T_{ph}$ . [12] Assuming a common lattice temperature for the various participating phonon baths, the elevated phonon temperature can be described by  $\Delta T_{ph} = P_{ph}/\kappa_0$ , where  $P_{ph}$  is the power absorbed by the phonon bath and  $\kappa_0$  is the out-of-plane thermal conductance in graphene. The former is simply the absorbed power from the laser if heat dissipation via the contacts is ignored, hence relatively independent of device temperature. On the other hand,  $\kappa_0$  increases with device temperature. Hence we expect a decreasing photo-excited phonon temperature  $\Delta T_{ph}$  with increasing device temperature  $\Delta T_{Joule}$  due to Joule heating. This is consistent with our experimental observation in (b). (c) We use a superlattice with 110 nm GNR width (a device we fabricated with bridges) to plot the gate voltage dependence of the photocurrent. The plasmon-phonon mode broadens by about 10% or 4V in FWHM when going from -2V to -10V in drain bias. Most of this broadening will be inhomogeneous broadening due to the more pronounced potential drop along the GNR superlattice at higher drain voltage. Electron and phonon lifetimes also decrease with increasing temperature and this should lead to a broadening of the hybrid plasmon-phonon mode in combination with a

reduction in peak height. The Joule heating at bias voltages of -2V and -10V translates into an increased device temperature of 1K and 15K respectively, which may lead to a small contribution to the broadening of a few percent. The associated decrease in resonance peak height can also play a contributing role in the observed decrease in photoconductance with increasing drain voltage (or device temperature) as shown in (b).



**Supplementary Figure S4: CVD process on copper foil produces single-layer graphene.** The Raman spectrum taken at  $\lambda=532$  nm shows a single Lorentzian G' band, indicating the presence of single-layer graphene. Our graphene is grown on copper foil, which is a process known for producing single-layer graphene almost exclusively.[45] The first layer grown passivates the copper surface and since the feedstock gas is supplied through the atmosphere, rather than being dissolved in the metal, no further layers are grown.



**Supplementary Figure S5: Electronic transport of graphene and superlattices with varying GNR width.** (a) Current-voltage characteristic of 2D graphene. (b-c) Current-voltage characteristic of GNR superlattices with GNR width as indicated. The 80 nm GNR superlattice contained bridges to guarantee current continuity. Electronic transport behaves p-type in air. We estimate from a combination of optical and electrical measurements a value of 52 V for the Dirac point gate voltage, which corresponds to a residual p-type doping of graphene of 0.33 eV. Superlattices with GNR width between 200 nm and 140 nm show similar transport behavior. Since we kept the fill factor (width/period) constant at 1/2, this indicates that electronic transport is essentially 2D as in graphene. All of these devices show reduction mode photocurrent as detailed in the main text, which is consistent with the situation in 2D graphene away from the Dirac point.[12] However, when going from 140 nm to 120 nm in GNR width, the transport current is reduced by about 30%, and going from 120 nm to 100 nm, it is reduced by another 50%. (The transport current of the 80 nm GNR superlattice is not directly comparable). The smaller GNR superlattices have more hopping transport character, with mobility limited by edge-roughness scattering and disorder, which can be described by a transport or mobility gap,[43,48] not to be confused with a real bandgap. In these narrow GNR superlattices, the enhancement mode photoconductivity becomes more important, especially at positive gate voltages close to the Dirac point. Figure 6 of the main text shows that in superlattices with GNR width of 100 nm and 80 nm, the photocurrent becomes indeed positive in a certain gate-voltage range approaching the Dirac point, indicating that the transport gap changes the photocurrent generation mechanism. In other words, the photocarriers increase the hopping transport along the localized states in disordered GNRs, and this effect overcomes the reduction due to increased phonon scattering.

## Supplementary Note 1: Calculating the RPA loss function

Here we describe the modeling of the loss function in graphene on SiO<sub>2</sub> as shown in the intensity plot of Fig. 3 in the main manuscript. We consider the interaction of the electronic degrees of freedom with graphene's internal optical phonon[49,50] and that due to the surface polar phonon on SiO<sub>2</sub>[40,51]. The plasmon response of graphene begins with finding the dielectric function where a satisfactory approximation can be obtained by adding the separate contributions *independently*. An effective interaction between electrons is given by the sum of the direct Coulomb interaction  $v_c(q) = e^2/2q\epsilon_0$  where  $q$  is the wave-vector. The two electrons interaction mediated by surface phonon and optical phonon are denoted by  $v_{sp,\lambda}(q, \omega)$  and  $v_{op}(q, \omega)$  respectively, where their explicit expressions are given elsewhere[31].

The RPA expansion of the dielectric function,  $\epsilon_T^{rpa}(q, \omega)$ , can be expressed with this effective interaction[41,52]

$$v_{eff}(q, \omega) = \frac{v_c(q)}{\epsilon_T^{rpa}(q, \omega)} = \frac{v_c(q) + \sum_{\lambda} v_{sp,\lambda}}{1 - [v_c(q) + \sum_{\lambda} v_{sp,\lambda}] \Pi_{\rho,\rho}^0(q, \omega)} \quad (S2)$$

where  $\Pi_{\rho,\rho}^0(q, \omega)$  is the non-interacting part (i.e. the pair bubble diagram) of the charge-charge correlation function given by a modified Lindhard function,[22,36]

$$\Pi_{\rho,\rho}^0(q, \omega) = -\frac{g_s}{(2\pi)^2} \sum_{nn'} \int_{\text{BZ}} d\mathbf{k} \frac{n_F(\xi_{\mathbf{k}}) - n_F(\xi_{\mathbf{k}+\mathbf{q}})}{\xi_{\mathbf{k}} - \xi_{\mathbf{k}+\mathbf{q}} + \hbar\omega} F_{nn'}(\mathbf{k}, \mathbf{q}) \quad (S3)$$

where  $n_F(\xi_{\mathbf{k}})$  is the Fermi-Dirac distribution function,  $F_{nn'}(\mathbf{k}, \mathbf{q})$  is the band overlap function of Dirac spectrum,  $g_s$  is the spin degeneracy. While the polar surface phonons couple to the charge density operator, the intrinsic optical phonon couple instead to the current operator. Its contribution to the dielectric function is given by  $v_{op}(q, \omega) \Pi_{j,j}^0(q, \omega)$ , where  $\Pi_{j,j}^0(q, \omega)$  is the current-current correlation function. We note that from the usual charge continuity equation,  $i\partial_t \hat{\rho}_{\mathbf{q}} = \mathbf{q} \cdot \hat{\mathbf{j}}_{\mathbf{q}}$ , it follows that,

$$q^2 \Pi_{j,j}(q, \omega) = \omega^2 \Pi_{\rho,\rho}(q, \omega) - v_F \left\langle \left[ \mathbf{q} \cdot \hat{\mathbf{j}}_{\mathbf{q}}, \hat{\rho}_{-\mathbf{q}} \right] \right\rangle \quad (S4)$$

where the second term in Eq.S4 is purely real and  $\propto q^2$  as calculated in Ref.[53]. The imaginary part of  $\Pi_{j,j}(q, \omega)$  can be obtained just from  $\Im[\frac{\omega^2}{q^2} \times \Pi_{\rho,\rho}(q, \omega)]$ . Collective modes with self consistent oscillations of the carrier charge can be obtained from the zeros of the



full dielectric function

$$\epsilon_T^{rpa}(q, \omega) = \epsilon_{env} - v_c \Pi_{\rho, \rho}^0(q, \omega) - \epsilon_{env} \sum_{\lambda} v_{sp, \lambda} \Pi_{\rho, \rho}^0(q, \omega) - \epsilon_{env} v_{op} \Pi_{j, j}^0(q, \omega) \quad (S5)$$

where  $\epsilon_{env}$  is the dielectric constant of graphene's environment. Damping is included phenomenologically through the following modifications;  $\Pi_{\rho, \rho}^0(q, \omega) \rightarrow \Pi_{\rho, \rho}^0(q, \omega + \tau_e^{-1})$ ,  $v_{sp, \lambda}(q, \omega) \rightarrow v_{sp, \lambda}(q, \omega + \tau_{sp}^{-1})$  and  $v_{op}(q, \omega) \rightarrow v_{op}(q, \omega + \tau_{op}^{-1})$ , where  $\tau_e^{-1}$ ,  $\tau_{sp}^{-1}$  and  $\tau_{op}^{-1}$  describes the electron, surface optical phonon and internal optical phonon lifetimes respectively. In this work,  $\tau_{sp}$  and  $\tau_{op}$  are phenomenological constants to be fitted to the experiments, while  $\tau_e$  is modeled rigorously, see below.

Here, we discuss model description of the electron lifetime  $\tau_e$ . Including relevant scattering mechanisms in our experiments,  $\tau_e$  is given by,

$$\tau_e(q, \omega) \approx [\tau_0^{-1} + \tau_{edge}(q)^{-1} + \tau_{ep}(\omega)^{-1}]^{-1} \quad (S6)$$

where  $\tau_0$  describes a background damping due to scattering with impurities and  $\tau_{edge}(q) \approx a/(W - W_0)^b$  is related to scattering off the ribbon edges.  $W$  is the ribbon's width and  $W_0$  accounts for the difference in physical and electrical widths. Experiments found this to be  $\approx 28 \text{ nm}$ [31].  $\tau_0 \approx 85 \text{ fs}$  as measured from the Drude response of large area, unpatterned graphene.  $a \approx 2 \times 10^6$ , of the order of Fermi velocity and  $b = 1$  as discussed in the main text.  $\tau_{ep}(\omega)$  is electron lifetime due to scattering with optical phonons. It is related to the electron self-energy  $\Sigma_{ep}$  via  $\tau_{ep} = \hbar/2\Im[\Sigma_{ep}]$ . According to density functional calculations, the imaginary part of  $\Sigma_{ep}$  can be approximated by,[54]

$$\Im[\Sigma_{ep}(\omega)] = \gamma_0 |\hbar\omega + \hbar\omega_0 + E_f| \times \frac{1}{2} \left[ \text{erf} \left( \frac{\hbar\omega - \hbar\omega_{op}}{\Delta_{ph}} \right) + \text{erf} \left( \frac{-\hbar\omega - \hbar\omega_{op}}{\Delta_{ph}} \right) + 2 \right] \quad (S7)$$

where  $\gamma_0$  describes the effective e-ph coupling and  $\Delta_{ph}$  accounts for various energy broadening effects such as the deviation from the Einstein phonon dispersion model. They are estimated to be  $\gamma_0 \approx 0.018$  and  $\Delta_{ph} \approx 50 \text{ meV}$  from density function calculations.[54]

Using the above theory, we plot the loss function in graphene on  $\text{SiO}_2$  as shown in Fig. 3 of the main manuscript. The calculations include interactions with the intrinsic and  $\text{SiO}_2$  substrate phonons. Graphene doping of  $E_f = -0.33 \text{ eV}$  and an effective  $\epsilon_{env} = 1.5$  is chosen to fit the plasmon modes determined from the extinction spectra. We assume a

typical  $\tau_{sp} = 1$  ps while a much smaller  $\tau_{op} = 70$  fs accounts for broadening effects due to finite phonon dispersion. Related to  $v_{sp,\lambda}(q, \omega)$  and  $v_{op}(q, \omega)$ , we have the frequencies of the various phonon modes at  $\omega_{op} = 1580 \text{ cm}^{-1}$ ,  $\omega_{sp1} = 806 \text{ cm}^{-1}$  and  $\omega_{sp2} = 1168 \text{ cm}^{-1}$ . Their respective electron-phonon coupling parameters used are  $g_0 = 7.7 \text{ eV \AA}^{-1}$ ,  $\mathcal{F}_{sp1}^2 = 0.2 \text{ meV}$  and  $\mathcal{F}_{sp2}^2 = 2 \text{ meV}$ .

### Supplementary References

- [46] Low, T., Perebeinos, V., Kim, R., Freitag, M. and Avouris, P. Cooling of photoexcited carriers in graphene by internal and substrate phonons. *Phys. Rev. B* **86**, 045413 (2012).
- [47] Freitag, M., Low, T. and Avouris, P. Increased Responsivity of Suspended Graphene Photodetectors. *Nano Lett.* **13**, 1644-1648 (2013).
- [48] Sols, F., Guinea, F. and Castro Neto, A. H. Coulomb Blockade in Graphene Nanoribbons. *Phys. Rev. Lett.* **99**, 166803 (2007).
- [49] Ando, T. Anomaly of Optical Phonon in Monolayer Graphene. *J. Phys. Soc. Jpn.* **75**, 124701 (2006).
- [50] Ishikawa, K. and Ando, T. Optical Phonon Interacting with Electrons in Carbon Nanotubes. *J. Phys. Soc. Jpn.* **75**, 084713 (2006).
- [51] Schiefele, J., Sols, F. and Guinea, F. Temperature dependence of the conductivity of graphene on boron nitride. *Phys. Rev. B* **85**, 195420 (2012).
- [52] Mahan, G. D. Many particle physics. (Springer, 2000).
- [53] Sabio, J., Nilsson, J. and Castro Neto, A. H. f-sum rule and unconventional spectral weight transfer in graphene. *Phys. Rev. B* **78**, 075410 (2008).
- [54] Park, C.-H., Giustino, F., Cohen, M. L. and Louie, S. G. Velocity Renormalization and Carrier Lifetime in Graphene from the Electron-Phonon Interaction. *Phys. Rev. Lett.* **99**, 086804 (2007).